

JGR Space Physics

RESEARCH ARTICLE

10.1029/2023JA032139

Key Points:

- Approximately 2.7% of the solar wind-sputtered sodium atoms directly contribute to the magnetospheric ions
- Cusp-originated sodium atoms can supply Na^+ ions to each magnetospheric region due to their sufficient initial velocity
- The pre-ionization transport of sodium atoms could potentially account for the observed dayside ring current Na^+ -group ions

Supporting Information:

Supporting Information may be found in the online version of this article.

Correspondence to:









Q.-G. Zong,
qgzong@pku.edu.cn

Citation:

Zhao, J.-T., Zong, Q.-G., Sun, W.-J., Zhou, X.-Z., Yue, C., Wang, S., et al. (2024). Dynamics of sputtered neutral sodium atoms in the near-Mercury space. *Journal of Geophysical Research: Space Physics*, 129, e2023JA032139. <https://doi.org/10.1029/2023JA032139>

Received 1 OCT 2023
Accepted 18 MAR 2024

Dynamics of Sputtered Neutral Sodium Atoms in the Near-Mercury Space

J.-T. Zhao (赵玖桐)¹ , Q.-G. Zong (宗秋刚)^{1,2} , W.-J. Sun (孙为杰)³ , X.-Z. Zhou (周煦之)¹, C. Yue (乐超)¹ , S. Wang (汪珊)¹ , J. A. Slavin⁴ , J. M. Raines⁴ , P. Wurz^{5,6} , and W.-H. Ip (葉永炬)^{2,7}

¹School of Earth and Space Sciences, Peking University, Beijing, China, ²State Key Laboratory of Lunar and Planetary Sciences, Macau University of Science and Technology (MUST), Macau, China, ³Space Sciences Laboratory, University of California, Berkeley, Berkeley, CA, USA, ⁴Department of Climate and Space Sciences and Engineering, University of Michigan, Ann Arbor, MI, USA, ⁵Space Research and Planetary Sciences, Physics Institute, University of Bern, Bern, Switzerland, ⁶NCCR PlanetS, University of Bern, Bern, Switzerland, ⁷Institute of Astronomy, National Central University, Zhongli, Taiwan

Abstract The solar wind sputtering in the magnetospheric polar cusp is an important source of heavy atoms in Mercury's exosphere and magnetosphere. However, the majority of ejected atoms are neutral, undergoing an extended period before photoionization occurs. In this study, we employ an ab initio simulation to investigate the behavior of sodium (Na) atoms prior to their photoionization. Our results reveal that overall only approximately 2.7% of the sputtered atoms contribute to magnetospheric ions, while the vast majority of these ions (~82.9%) escape into interplanetary space. The remaining fraction (14.4%) eventually returns to the planetary surface. For Na atoms ionized inside the magnetosphere, a larger proportion of Na^+ (53.5%) is supplied to the magnetotail compared to the polar cusp (39.4%), which is due to the tailward acceleration caused by solar radiation. Additionally, the remaining Na^+ (7.1%) contributes to the dayside ring current region, as demonstrated by the observation of the MExcury Surface, Space ENvironment, GEochemistry, and Ranging (MESSENGER) spacecraft. Our research introduces a perspective on Na^+ transport in the magnetosphere that complements and coexists with traditional mechanisms.

Plain Language Summary Mercury's exosphere and magnetosphere contain various heavy planetary elements. These elements are released from the planet's surface due to different space weathering processes. One notable process is the direct bombardment of the solar wind ions on the planetary surface through open magnetic field lines (i.e., the polar cusp), which releases neutral atoms with low energies around ~eV. Our simulation results indicate that these low energy ~eV atoms may travel a significant distance before their photoionization or return to the surface. Consequently, Na atoms originating from the polar cusps can supply ions to different regions in the vicinity of Mercury. This mechanism offers an explanation for the concentration of sodium group ions in the dayside ring current, as observed by MESSENGER.

1. Introduction

Mercury, the closest planet to the Sun, has an intrinsic dipole field like Earth with a magnetic momentum of $195 \text{ nT} \cdot \text{R}_M^3$ (R_M , Radius of Mercury, 2,439 km). Its dipole tilt angle is negligible ($<0.3^\circ$), but its dipole center is shifted northward by 0.196 R_M (Alexeev et al., 2010; Anderson et al., 2010, 2011). Mercury's magnetosphere is tightly compressed, and the subsolar stand-off distance of its magnetopause is only $\sim 1.45 \text{ R}_M$ due to the high solar wind ram pressure and relatively weak intrinsic magnetic field (Siscoe et al., 1975; Slavin, Acuna, et al., 2009; Slavin, Anderson, et al., 2009; Winslow et al., 2013). The polar cusps near the northern and southern poles stand as the most direct entry point for solar wind in this magnetosphere.

Given Mercury's lack of a substantial atmosphere, incoming solar wind particles can directly bombard its surface. This impact releases mostly neutral atoms ($>90\%$) and some ions ($\sim 5\% - 10\%$) from the surface (Hofer, 1991), while the sputter yield could be highly variable (Wurz et al., 2022). Compared to the other space weathering processes (e.g., photon-stimulated desorption, micro-meteoroid impact vaporization), solar wind sputtering releases particles with much higher initial kinetic energies ($\sim \text{eV}$) (Gamborino et al., 2019; Wiens et al., 1997; Wurz & Lammer, 2003; Ziegler et al., 2010). These sputtered particles contribute significantly to Mercury's upper exosphere and magnetosphere (Ip, 1986), especially during the transit of coronal mass eject (Orsini et al., 2018).

However, it is noteworthy that the observation from the Mercury Atmospheric and Surface Composition Spectrometer instrument onboard Mercury Surface, Space Environment, Geochemistry, and Ranging (MESSENGER) spacecraft shows the year-to-year variability of the global sodium distribution is small (Cassidy et al., 2015; Mangano et al., 2015). So, the solar wind sputtering of sodium atoms is only dominant at some specific regions, such as the polar cusp and the upper exosphere.

The sputtered sodium atoms prominently absorb and emit solar radiation at wavelengths of 589.0 nm (D1 line) and 589.6 nm (D2 line). As the solar wind ion sputtering relates closely to space weather events like coronal mass ejections, the pattern of sodium D1/D2 emissions can offer insights into these events (Orsini et al., 2018).

In addition to solar wind ions and sputtered neutral atoms, heavy planetary ions (e.g., Na⁺, O⁺) are concentrated around the polar cusp. Their densities are comparable to alpha particles (Raines et al., 2014; Sun et al., 2022). Sun et al. (2022) noticed these heavy ions stretch from the northern polar cusp to the subsolar ring current region (Fu & Zong, 2022; J. T. Zhao et al., 2022; Zong et al., 2022). This equatorward expansion of planetary ion distribution is attributed to the frequent newly reconnected, twisted magnetic field lines and the precipitated ions accompanied within it. In this scenario, the ring current Na⁺-group ions are believed to originate from the sputtered Na⁺.

However, the entry of the heavy ions from the polar cusp to the dayside ring current is also detectable during non-flux transfer event (non-FTE) shower intervals (Sun et al., 2022). Besides, the contribution from the sputtered neutral atoms has yet to be examined. Hence, the planetary particle dynamics around the cusp desire further investigation.

Our study explores the dynamics of sputtered neutral atoms before they get photoionized. We employ an ab initio simulation to provide a statistical overview of this process. Both observations by the MESSENGER spacecraft and the magnetic field model are used to constrain the simulation setup. The Na⁺ supply rate to the magnetosphere due to sputtering can be obtained by releasing neutral atoms within the polar cusp and tracing their trajectories. A further full-Lorentz test particle simulation is implemented to demonstrate the distribution of the Na⁺ originating from solar wind sputtering. In the last two sections, we discuss the implications of this scenario and the possible improvement of this model.

2. Data Set and the Magnetic Field Model

2.1. MESSENGER Density Observation

This study uses data from the Fast Imaging Plasma Spectrometer (FIPS) onboard MESSENGER (Andrews et al., 2007). FIPS captured the energy spectrum of five ion types: H⁺, He⁺, He²⁺, the O⁺-group (with a mass-to-charge ratio, m/q, ranging from 14 to 20 amu/e), and the Na⁺-group (with m/q between 21 and 30 amu/e). These ions were measured across an energy-per-charge range of 46 eV/e to 13.6 keV/e. The field of view (FOV) of the FIPS spans approximately 1.15π sr, and it collects data at a 10-s cadence. By integrating the phase space density inferred from the energy spectrum data, we can determine the observed number density for each ion species:

$$n_{obs,s} = \sum_i f_{i,s} v_{i,s}^2 (\Delta v_{i,s}) (\Delta \Omega_{i,s}) \quad (1)$$

where $n_{obs,s}$ is the observed density, $f_{i,s}$ is the ion phase space density, $v_{i,s}$ denotes the velocity, $\Delta v_{i,s}$ is the width of the energy channel in the velocity domain, and the $\Delta \Omega_{i,s}$ is the solid angle of FIPS's FOV. The subscript "i" and "s" indicate the index of the energy channel and the ion species from the FIPS, respectively. Due to instrument limitations on energy range and FOV limitations arising from spacecraft obstructions, the observed density might be less than the actual ion density. According to the measurement by Raines et al. (2014) and Sun et al. (2022), the Na⁺-group ion energy is ~keV and the potential deviation from the actual ion density could be not significant. While, James et al. (2019) suggests the existence of high-density cold ions based on the observation of field line resonance. A significant cold portion cannot be ruled out yet. Nonetheless, this observed density can still illustrate the degree of ion concentration. In this study, we use it to standardize the statistical results across different ion species. Apart from the Na⁺-group ions, the He²⁺ ion is taken as a tracer of the solar wind to illustrate the solar wind ion precipitation and sputtering.

Using the spatial superposition analysis method (J.-T. Zhao et al., 2020), we illustrate the spatial distribution of observed densities for He²⁺ (top two panels) and the Na⁺-group ions (bottom two panels) in Figure 1. The panels

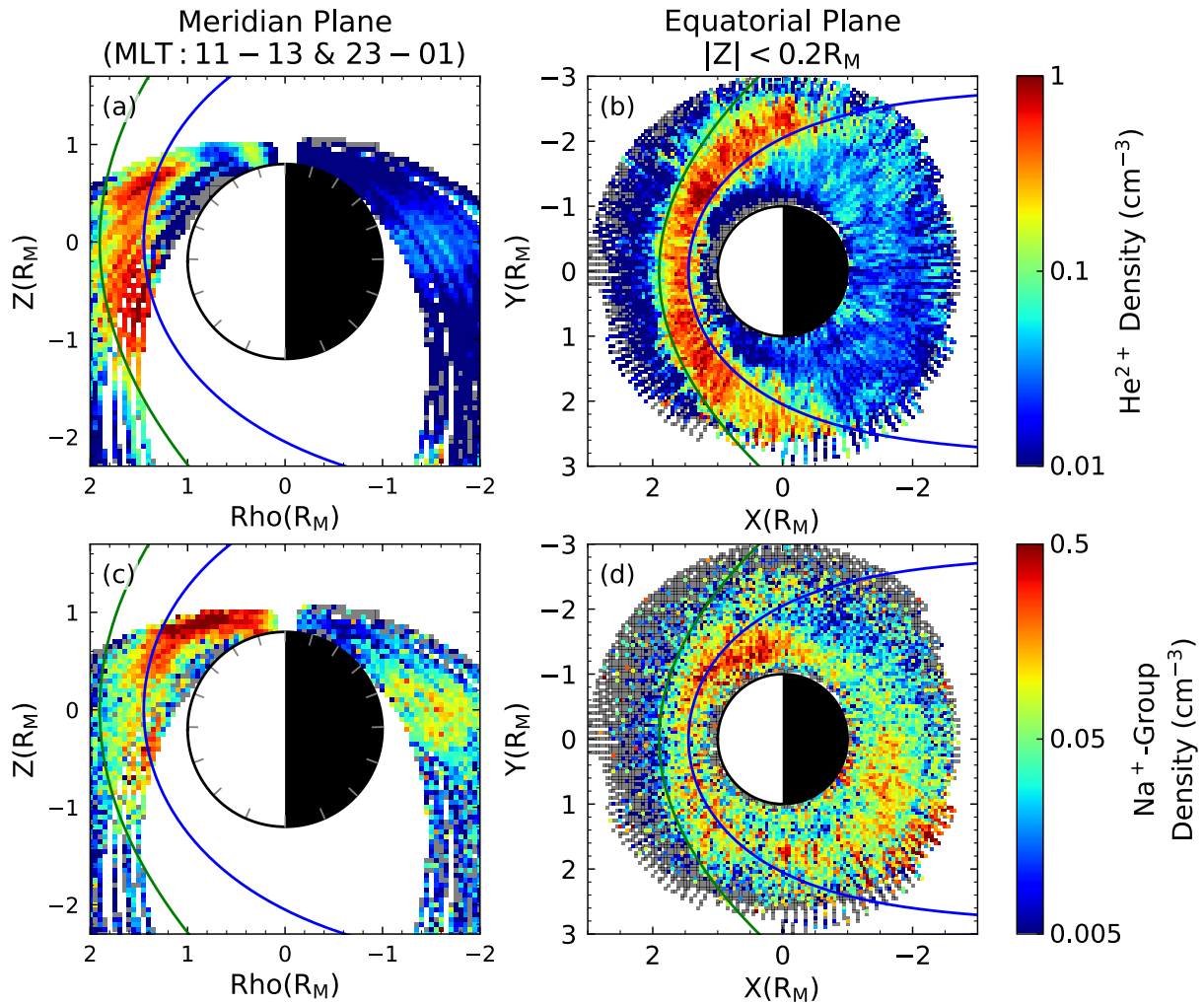


Figure 1. Density distribution of He²⁺ and the Na⁺-group ions as observed by FIPS/MESSENGER. Panels (a) and (c) depict the spatial distribution within the noon-midnight meridian plane ($Rho = \text{sign}(X) \cdot \sqrt{X^2 + Y^2}$). Panels (b) and (d) showcase the distribution within the magnetic equatorial plane. The modeled bow shock and magnetopause are represented by green and blue solid lines, respectively (Winslow et al., 2013). Gray ticks inside the planet indicate the MLATs range from -90° to $+90^\circ$, with a step of 20° .

on the left depict the distribution measured by MESSENGER within the noon-midnight meridian plane ($11 \text{ hr} < \text{MLT} < 13 \text{ hr}$ or $23 \text{ hr} < \text{MLT} < 01 \text{ hr}$, where MLT stands for magnetic local time), while the panels on the right display the distribution within the magnetic equatorial plane ($|Z| < 0.2 R_M$, in the aberrated Mercury-Sun Magnetospheric (aMSM) coordinate system as defined in J. T. Zhao et al. (2022)). The observations and simulations mentioned below will be present in the aMSM coordinate system. All the FIPS measurements within the orbiting mission duration are taken into account except for the period with solar energetic electron events (Gershman et al., 2015). It means that the observation represents an average-state distribution of the ion density to some extent. The He²⁺ distribution prominently highlights the entry point of the solar wind at a magnetic latitude (MLAT) of $\sim 70^\circ$. The Na⁺-group ions distribution further indicates concentrations in the off-equator (subsolar) and equatorial (pre-noon) ring current region. The dawn-dusk asymmetry of Na⁺-group ions density in the equatorial plane demonstrates the western drift motion of the heavy ions.

2.2. KT17 Magnetic Field Model

We use the KT17 magnetic field model to trace magnetic field line topology and evaluate the ion trajectory (Korth et al., 2017). This model relies on two independent input variables: the disturbance index (DI, ranging from 0 to 97) and Mercury's heliocentric distance (r_{hel} , ranging from 0.307 AU to 0.467 AU). For our analysis, we opted for

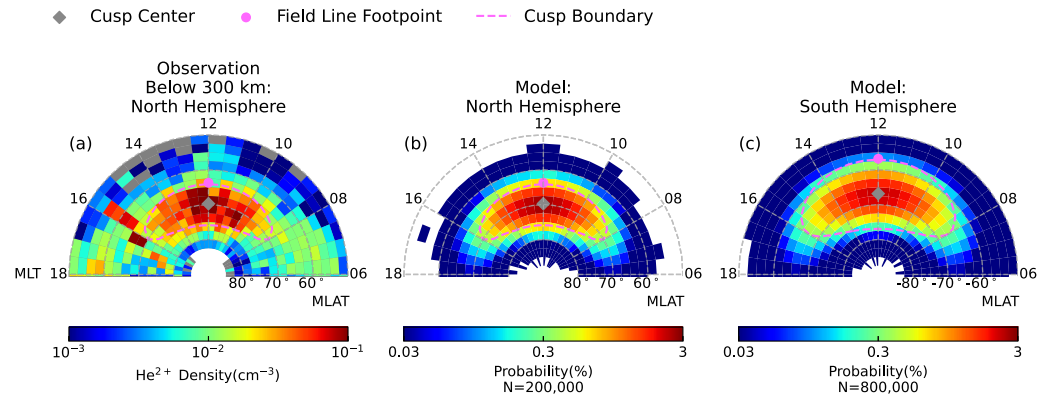


Figure 2. Spatial distribution of the He^{2+} ions observed density and the Na simulated production rate. Panel (a) displays the measured spatial distribution of He^{2+} at altitudes below 300 km. Panels (b and c) illustrate the modeled spatial distribution of Na atoms released during our simulation initialization in the magnetic northern ($Z > 0$) and southern ($Z < 0$) hemispheres, respectively. These patterns are normalized based on the total count of test atoms: 200,000 in the north and 800,000 in the south. Gray diamonds denote the centers of the cusps (MLATs of 70° and -67°), while the boundaries of the cusps are shown as magenta dashed lines. A pair of conjugate footprints of the magnetic field lines are represented with magenta dots. The nightside observed distribution of He^{2+} ions, which is shown in Figure S1 of the Supporting Information S1, reveals the polar cusp is the primary sputtering source. He^{2+} ions are used as a tracer of solar wind ions in this study.

median input parameters ($DI = 50$ and $r_{\text{hel}} = 0.387$ AU) to manifest a magnetosphere influenced by a moderate external driving source. Note that the KT17 is a static model, not accounting for temporal variations or induction effects (Glassmeier et al., 2007; Slavin, Acuna, et al., 2009; Slavin, Anderson, et al., 2009). In theory, the time-varying electromagnetic field may lead to the acceleration and pitch angle scattering of the ions and is unfavorable for the trapping of ring current ions. Also, the average-state magnetosphere is less compressed than the magnetosphere under intense solar wind enforcement when the solar wind precipitation flux is also higher. Hence, our simulated ion lifetime and density could be higher than the realistic values.

3. Simulation Setup and Result

3.1. Neutral Atom Dynamics

We utilize the Monte Carlo method in our simulation to optimize computational efficiency. We randomly released 1,000,000 test Na atoms from the planetary surface surrounding the polar cusp. The initial positions of these atoms are dictated by a two-dimensional normal distribution (Equation 2) aligned with MLT and MLAT:

$$P(\text{MLT}, \text{MLAT}) = \frac{1}{2\pi \Delta\text{MLT} \Delta\text{MLAT}} \cdot \exp \left[-\frac{1}{2} \left(\frac{\text{MLT} - 12}{\Delta\text{MLT}} \right)^2 - \frac{1}{2} \left(\frac{\text{MLAT} - \text{MLAT}_{\text{cusp}}}{\Delta\text{MLAT}} \right)^2 \right] \quad (2)$$

where $P(\text{MLT}, \text{MLAT})$ is the probability distribution function of the atom's initial MLT and MLAT. Taking cues from MESSENGER's observation of He^{2+} density near the dayside planetary surface (as seen in Figure 2a), we designate the MLAT of the northern cusp center ($\text{MLAT}_{\text{cusp}}$) as 70° . For the northern cusp, we empirically set the variances of MLT (ΔMLT) and MLAT (ΔMLAT) to 2 hr and 3° , respectively. The cusp boundaries are demarcated at the contour where the probability distribution function reduces to $1/e^2$ of the peak probability. The MLAT for the southern cusp is deduced by tracing a closed magnetic field line from the northern cusp boundary to the southern surface (magenta dots in panels a–c). ΔMLAT for the southern hemisphere is set to 5° to ensure the magnetic flux inside both cusps are comparable (0.29 and 0.31 MWb for the northern and southern cusps, respectively). The cusp boundaries are shown as magenta dashed lines.

Owing to the north-south asymmetry in Mercury's magnetic dipole, the magnetic field intensity at the northern cusp (~ 631 nT, based on the model intensity at a MLAT of 70°) is roughly three times stronger than at the southern cusp (~ 163 nT, based on the model intensity at a MLAT of -67°). Consequently, 20% of the test atoms are released from the northern cusp, while the southern cusp accounts for the remaining 80% (Anderson et al., 2011; Gamborino et al., 2019). Figures 2b and 2c show the probability distribution of 1,000,000 test atoms

in the northern and southern hemispheres. About 86.5% ($1-e^{-2}$) of the test atoms are released inside the cusp region we identified in Figure 2. The rest of the test atoms would be excluded from our simulation because of our investigation aim.

The initial energy distribution of the ejected atoms we adapted is as follows (Wurz & Lammer, 2003):

$$f(E) \propto \frac{E}{(E + E_b)^3} \left\{ 1 - \left[\frac{E + E_b}{E_{in}} \right]^{\frac{1}{2}} \right\} \quad (3)$$

where E is the energy of the sputtered atom, E_b is the surface binding energy (which is set to 2.0 eV, (Ziegler et al., 2010)), E_{in} is the bulk energy of the incident ion (aligned with the typical solar wind H^+ bulk energy, 1 keV). It is worth mentioning that the sodium surface binding energy has yet to be clearly identified and may vary from 0.27 eV (sodium sulfate, Na_2SO_4) to 8.4 eV (jadeite, $NaAlSi_2O_6$) depending on minerals (Morrissey et al., 2022). The value we adopt here is a relatively medium one. The sputtering difference between solar wind ion species and the incident energy fluctuation are not considered here as the sputtering energy spectrum is almost the same except for the \sim keV high energy tail. The ejection angle, relative to the local surface's normal direction, follows a probability distribution proportional to its cosine value. As for the azimuth angle of the ejected atoms, it follows a uniform distribution ranging between 0° and 360° .

We subsequently refine the particle distribution by iterating through the equation of motion (Equation 4) using a time step (Δt) of 1 s:

$$\frac{d^2 \mathbf{r}}{dt^2} = -\frac{GM_{Mercury}}{r^2} \hat{\mathbf{r}} + \mathbf{a}_{rad} \quad (4)$$

In the equation, the first term on the right-hand side denotes the gravitational acceleration, while the second term, labeled as \mathbf{a}_{rad} , signifies the anti-sunward acceleration due to solar radiation. The value of \mathbf{a}_{rad} is dependent on the heliocentric distance ($\propto r_{hel}^{-2}$) and the radial velocity of the atom relative to the Sun (i.e., Swings effects). The relationship between the radiation acceleration and the relative radial velocity is given in Figure S2 of the Supporting Information S1. Another crucial dynamic aspect is the photoionization of the Na atom. Rather than treating photoionization as a stochastic process, it's modeled as a continuous one to simplify computation in our simulation (Wang & Ip, 2011). We assign each test atom a dimensionless initial weight (w) indicative of its density. As photoionization proceeds, this weight diminishes over time, described by $w(t + \Delta t) = w(t) \exp(-\frac{\Delta t}{\tau})$, where τ is the photoionization period (i.e., the inverse of the photoionization rate, 5.07×10^{-5} /s at 0.387 AU, scaled from the photoionization rate at 1 AU under medium solar activity given by <https://phidrates.space.swri.edu/>), Δt (1 s) is the time step. Concurrently, the attenuated portions, $\Delta w(t + \Delta t) = w(t) \exp(-\frac{\Delta t}{\tau}) \Delta t$ contribute to the ion supply rate in Mercury's vicinity. It is worth mentioning that the radiation acceleration and photoionization (also, the weight decay) of the Na only occur outside of Mercury's shadow.

When the atoms encounter the planetary surface, they are considered as "returned atoms" and excluded from subsequent motion iterations. Similarly, the atoms that encounter the simulation boundary ($X, Y, Z = \pm 3 R_M$) are considered as "escaped atoms" and excluded from the subsequent iterations because they are not likely to contribute Na^+ ion to the inner magnetosphere. After a sufficiently long time, the escaped portion is expected to be photoionized in the interplanetary space or the distant magnetotail. The simulation time is at most six photoionization periods. After this duration, most of the neutral atoms have either been photoionized or have returned to the planetary surface.

We totally execute 12 neutral atom simulations at different true anomaly angles (TAA = $0^\circ, 30^\circ, \dots, 330^\circ$). The radiation acceleration, the Doppler effect, and the photoionization rate are considered separately in each simulation run. The simulated ion supply rates are shown in Figures 3a–3d. These simulation results are available online (J. Zhao, 2024).

The simulated supply rate shows seasonal variation, especially in the downstream region. Owing to the proportionality between the solar wind density and r_{hel}^{-2} , the Na^+ supply rate distribution is scaled by $(0.387 \text{ AU}/r_{hel})^2$. Three characteristic trajectories of the neutral atoms are shown as pink solid lines. These atoms are released at the northern polar cusp with an initial energy of 2.0 eV and initial ejection angles of $-85^\circ, 0^\circ$, and

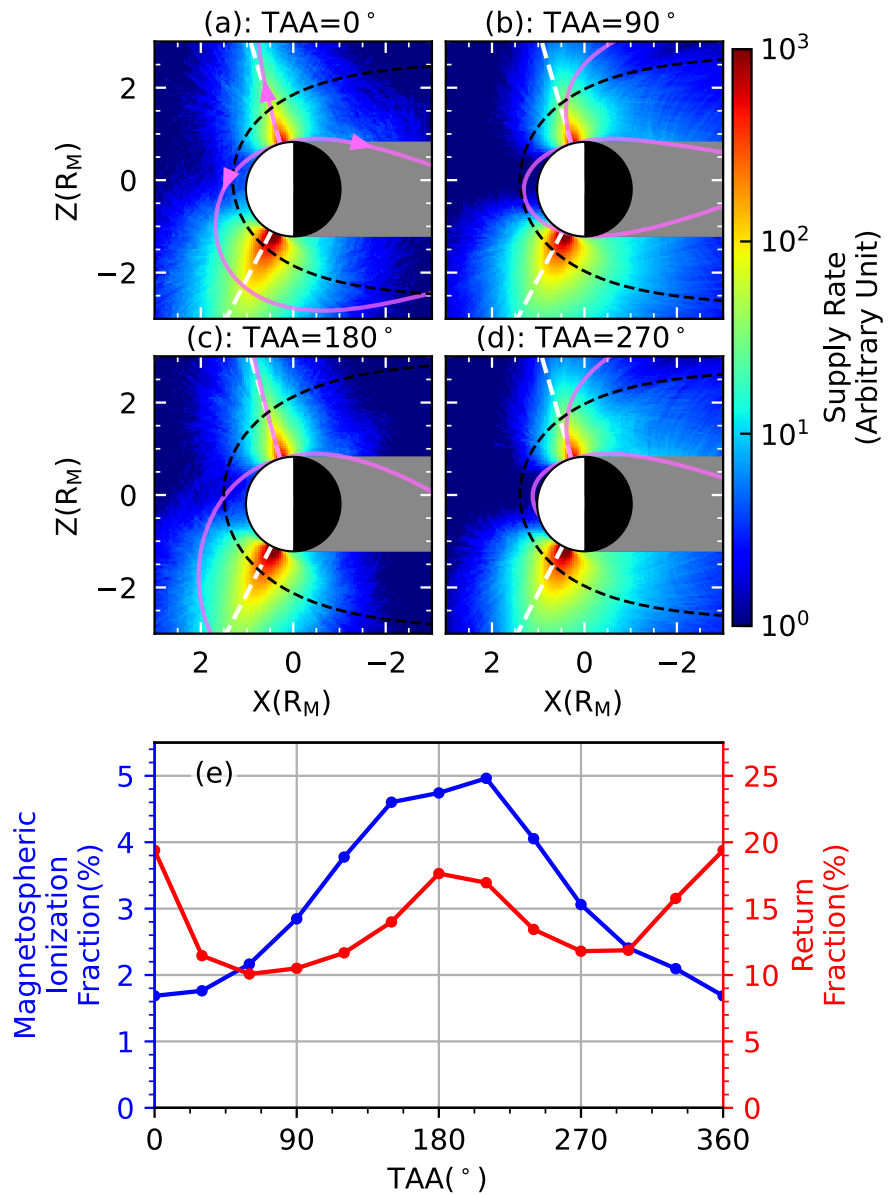


Figure 3. Neutral Na atom simulation results at different true anomaly angles. (a–d) The meridional distribution ($|Y| < 0.2 R_M$) of the ion supply rate at TAA = 0°, 90°, 180°, and 270°, respectively. We employ an arbitrary unit here, focusing on the spatial distribution, especially when the Na atom sputter yield remains uncertain. (e) The fraction of the Na atoms that returns to the planetary surface (red solid line) and that ionizes inside the magnetosphere (blue solid line). Pink solid lines in the first four panels demonstrate the characteristic trajectories of the Na atoms. White dashed lines indicate the local surface’s normal direction.

+85° (with zero velocity along the Y-direction). It should be mentioned that the sputtering ejection angles peak at 0°, and the atoms with large ejection angles only occupy a small fraction. It can be seen that the radiation acceleration is decisive for the motion of sodium atoms. A distribution at a specific TAA is not representative of an average-state condition.

The fraction of the returned Na atoms and the ionized atoms inside the magnetopause (black dashed lines in panels a–d) is plotted in panel e. The return fraction decreases as the tailward acceleration increases at the TAA of ~90° and ~270°. As for the ionization fraction inside the magnetosphere, the size of the magnetosphere is more deterministic. The magnetopause has a parabolic shape and its subsolar distance is proportional to $r_{hel}^{1/3}$ (Korth et al., 2017; Winslow et al., 2013). Therefore, this value approaches the maximum near the aphelion

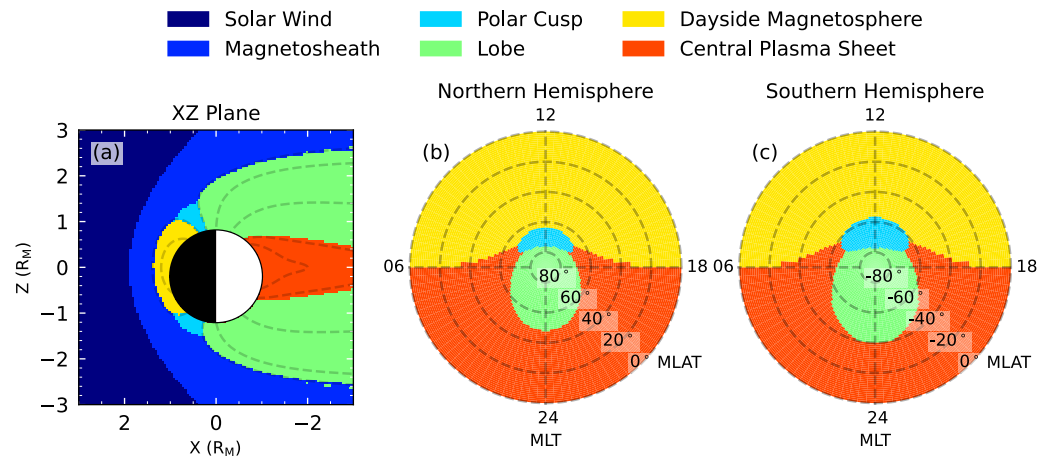


Figure 4. Magnetospheric regional partition based on the KT17 model. (a) Partition representation in the XZ plane ($Y = 0$). (b, c) Partitions visualized in the MLAT-MLT coordinates for the northern hemisphere (b) and southern hemisphere (c).

(TAA = 180°). On average, 14.4% of released atoms finally return to the planetary surface. Here, the inverse of the orbital angular velocity is used as a weight when averaging the above fractions. Meanwhile, 2.7% of released atoms are ionized within the magnetosphere. The remaining 82.9% either escape or ionize out of the near-Mercury magnetosphere (magnetosphere grid bins with $|X|, |Y|, |Z| < 3 R_M$). Similarly, the weighted average supply rate will be used in the following calculation as it exemplifies average-state values. Figure 5a illustrates the weighted averaged Na^+ supply rate distribution in the noon-midnight meridian plane ($|Y| < 0.2 R_M$).

To analyze the transport of cusp-originated sodium to other magnetospheric regions quantitatively, we partition the near-Mercury environment ($|X|, |Y|, |Z| < 3 R_M$) into distinct zones: solar wind, magnetosheath, polar cusp, magnetotail lobe, dayside magnetosphere, and the central plasma sheet. The solar wind, magnetosheath, and magnetosphere are separated by the modeled bow shock and magnetopause, respectively (Winslow et al., 2013). We trace the model's magnetic field line to classify a grid bin ($\Delta X = \Delta Y = \Delta Z = 0.05 R_M$) within the magnetosphere. If the magnetic field line footprint of a grid bin falls within our predefined cusp boundaries, that bin is designated as the polar cusp. However, certain near-magnetopause positions can also be traced to the polar cusp (see Figure 3 of Tsyganenko and Russell (1999)). Therefore, positions are classified as the magnetosheath instead of the cusp when the inward magnetic field line length surpasses $1.2 R_M$ and $0.7 R_M$ in the northern and southern hemispheres, respectively. Regions where the magnetic field line connects to the distant tail ($X < -10 R_M$) are labeled as the magnetotail lobe. The remaining regions, covered by closed magnetic field lines, are further subdivided based on the MLT at which their field lines intersect the magnetic equator. Figure 4 illustrates this partitioning of the space near Mercury.

Combining with the region partition and the averaged Na^+ supply rate, we present the supply fraction to each magnetospheric sub-region in Table 1. Our findings reveal that neutral atoms originating from the cusp undergo photoionization across all magnetospheric sub-regions. The total Na^+ supply for these regions can be given by integrating the supply rate in the corresponding grid bins. Due to the tailward radiation acceleration, a significant portion of the ionization occurs in the magnetospheric lobe (43.4%) and the central plasma sheet (10.1%). Meanwhile, a considerable fraction (7.1%) of the ionized atoms directly “penetrate” into the dayside closed field line region from the polar cusp. Furthermore, 39.4% of the ionizations are confined within the polar cusps.

3.2. Ionized Atom Dynamics

It is necessary to emphasize that the total supply rate (Q) obtained from our simulation is different from the directly measured ion density by MESSENGER. To bridge this gap, we adopt the method proposed by Delcourt et al. (2003) to establish a connection between the ion supply rate and the ion density. Specifically, we release a single test particle with a random initial velocity within each magnetospheric grid bin and trace its trajectory in the magnetic field model in each simulation run. We can get the density contribution from each test particle by calculating its residence time in each grid bin. We sum up the contributions across all released test particles and then are weighted by the supply rate at the release grid bin, yielding the global density distribution. This process is

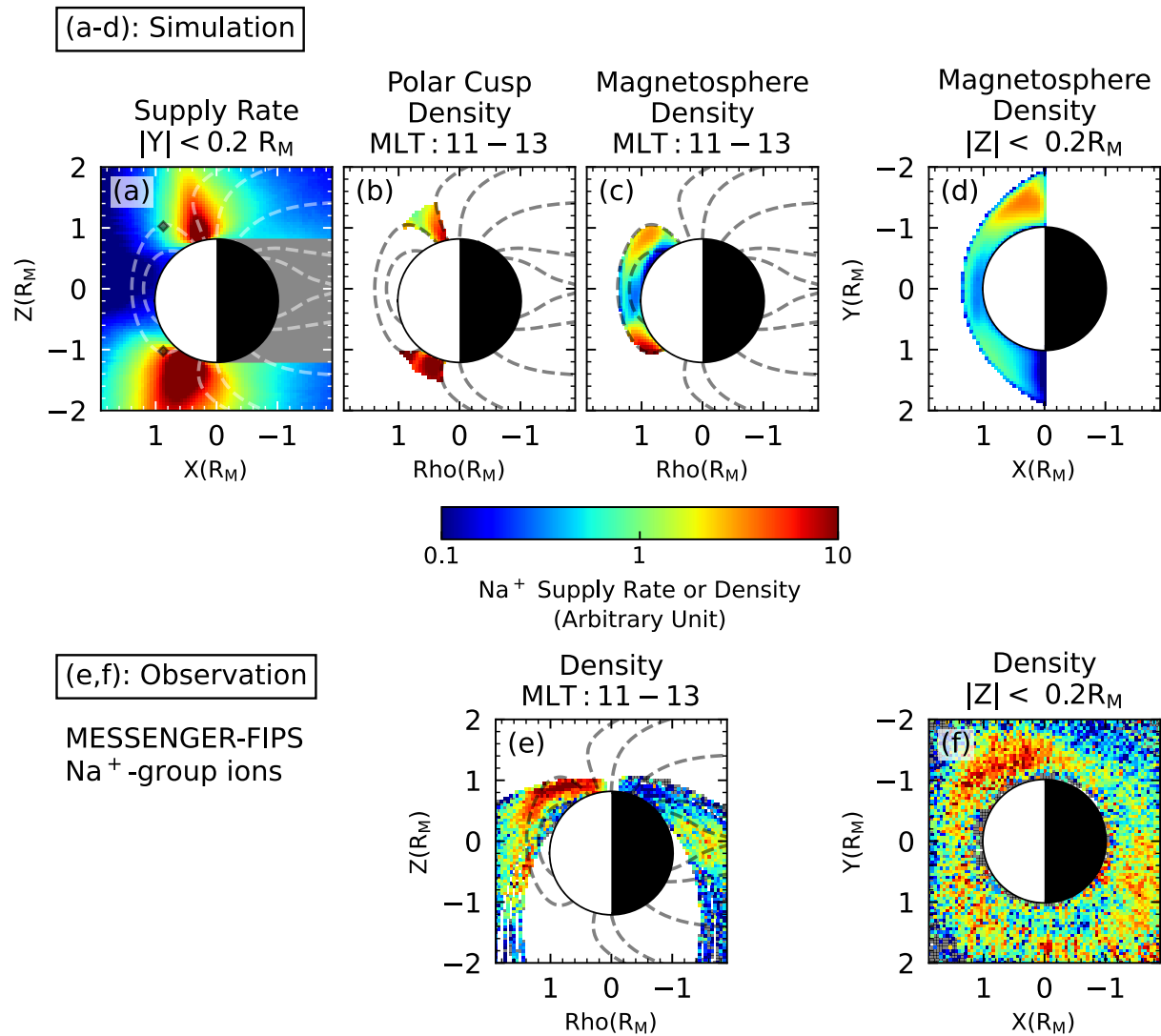


Figure 5. Simulated Na^+ supply rate and density. (a) Simulated Na^+ supply rate in the noon-midnight meridian plane. (b) Simulated Na^+ density within the polar cusp. (c) Simulated Na^+ density within the dayside ring current. (d) Simulated Na^+ density in the equatorial plane. (e, f) Adapted from Figures 1b and 1d.

Table 1

Na^+ Supply Rate to Different Magnetospheric Regions, See Figure 4

Region	Total supply (arbitrary unit)	Volume (R_M^3)	Supply per volume (arbitrary unit)	Fraction to the magnetospheric supply
Solar Wind	135.0	80.3	1.7	–
Magnetosheath	289.5	81.3	3.6	–
Polar Cusp	87.3	0.4	201.8	39.4%
Lobe	96.2	27.0	3.6	43.4%
Dayside Magnetosphere	15.8	4.3	3.7	7.1%
Central Plasma Sheet	22.4	23.9	0.9	10.1%
Out of Boundary ($ X , Y , Z = 3 R_M$)	7,916.2	–	–	–

Note. The volume of each region is present by counting the grid bins that belong to each zone. The supply per volume and the total supply represent the average and the summation of the supply rate within each zone. The fraction of the atoms out of the simulation boundary of $3 R_M$ is shown in the last row.

repeated 100 times with different random initializations and the average of the 100 results provides the simulated global density distribution. Furthermore, the standard deviation across these 100 runs serves as an indicator of the error of this simulation algorithm.

Unlike neutral atoms, ions are primarily driven and controlled by electromagnetic force. Following photoionization, ions experience various energization processes, including centrifugal and wave-ion resonant accelerations (Delcourt et al., 2002, 2003, 2012; Raines et al., 2014). Observations in Glass et al. (2021), Raines et al. (2014), and Sun et al. (2022) show that the thermal energy of the observed Na⁺-group ions in the polar cusp and dayside ring current is approximately 1 keV, which indicates a localized and rapid energization process. Otherwise, we would not expect to observe these energetic Na⁺ near their source region. Furthermore, this energization process must be mostly non-adiabatic, as the adiabatic energization from ~eV to ~keV would result in ion pitch angles falling within the bounce loss cone. However, a comprehensive understanding of these energization processes for planetary ions remains an open research. Additionally, neither in situ observations nor a verified analytic model of the electric field have been presented thus far.

Due to the complexities, our simulation does not include the electric field and energization processes. Instead, we directly assign an initial energy to the released ions. The validity and influence of this approximation will be discussed in the discussion section. Specifically, the ions' initial kinetic energy (W) follows a Maxwellian distribution with a temperature of 1 keV, as shown by Raines et al. (2014). Moreover, based on the pitch angle distribution provided by Sun et al. (2022) (refer to Figure S3 in Supporting Information S1), the initial pitch angle (α) follows a probability function proportional to the fourth power of the sine of the pitch angle ($\sin^4\alpha$).

The test particle simulation for the Na⁺ is conducted with the 4th-order Runge-Kutta algorithm with an adaptive timestep (1/100 of the local gyro period). In this simulation, we employ trilinear interpolation to speed up the calculation of the model magnetic field. The mesh grid resolution is set to be 0.02 R_M and the error metrics, specifically, the minimum, lower quantile, medium, upper quantile, the maximum of the absolute error (|Model Value—Interpolated Value|) are 0.002, 0.2, 0.5, 1, and 20 nT, respectively. Our primary objective is to interpret MESSENGER's observations of the dayside magnetosphere using our model. Therefore, the simulation terminates when an ion collides with the planetary surface, transfers into the nightside magnetosphere, or enters the magnetosheath.

3.3. Simulation Result and Comparison to the Observation

Averaging the simulation results in the 100 runs, we present the simulated ion density distribution in Figures 5b–5d. This format provides a more direct comparison with the observations from the MESSENGER spacecraft, as illustrated in Figures 5e and 5f. The density within the subsolar ring current region is comparable to that within the northern polar cusp, as demonstrated by both the observation and simulation. In our simulation result, the Na⁺ density in the dayside ring current is lower than that in the northern polar cusp, indicating the possible existence of other Na⁺-group ions sources or the Na⁺ lifetime is underestimated. Some possible explanations will be discussed in the following section. The simulated Na⁺ density in the equatorial plane (Figure 5d) accumulates as the Na⁺ drifts westward, displaying the dawn-dusk asymmetry. Such a dawn-dusk asymmetry is also a clear and key feature in the observational distribution of Na⁺-group ions (Figure 5f). The standard deviation of the simulation results of the 100 runs is shown in Figure S4 of the Supporting Information S1, and the uncertainty (~10%) is acceptable overall.

In summary, our simulation is capable of explaining the entrance of cusp-originated Na⁺ to the dayside ring current.

4. Discussion

This study focuses on the pre-ionization dynamics of the Na atoms sputtered by the solar wind ions within Mercury's cusp. As the photoionization rate is significantly low and the released Na atoms have velocities comparable to the escape velocity, a significant fraction of the sputtered Na atoms travel away from the cusp and supply Na⁺ to the regions of the magnetosphere other than the cusp. Through a test particle simulation, we convert the simulated ion supply rate into a density distribution that aligns with the Na⁺-group ions concentration in the dayside ring current, as observed by MESSENGER. About 2.7% of sputtered atoms eventually contribute planetary ions to the magnetosphere. This low ionization ratio suggests that the sputtered ion (with a yield of 5%–

10% compared to the sputtered atom) cannot be ignored. Moreover, the unconsidered supply to the magnetosheath and upstream solar wind might return to the magnetosphere through polar cusp, magnetic reconnection, or other mechanism (Glass et al., 2021).

In the following, we will consider the limitations of both the observations and simulations.

4.1. Limitation of the Observations

The FIPS measurements can not provide the true density due to its incomplete energy and angular coverage. This limitation can be eliminated to some extent as the thermal energy of the magnetospheric Na⁺-group ions (0.1–1 keV) is still within the energy range of the FIPS (Gershman et al., 2014; Raines et al., 2014; Zurbuchen et al., 2011). Also, the Na⁺-group observed density is contributed by other species with m/q ranging from 21 to 30 amu/e (e.g., Mg⁺, Si⁺). These species may possess distinct characteristics, including different photoionization rates and surface binding energies. The only m/q spectrum given by Wurz et al. (2019) and Zurbuchen et al. (2008) highlights a non-ignorable secondary count peak near the m/q of 28. In the matter of Na⁺, distinguishing between photoionized sputtered neutral atoms and sputtered ions remains challenging at present. It is expected that the BepiColombo spacecrafts, arriving at Mercury in December 2025, will provide more accurate and detailed sodium measurements with its Mercury Sodium Atmospheric Spectral Imager (MSASI) and Mercury Plasma Particle Experiment (MPPE) (Saito et al., 2010; Yoshikawa et al., 2010), covering the neutral and ionized states of the sodium.

4.2. Limitation of the Simulations

Prior research on the neutral atom dynamics has exhibited the accuracy and efficiency of the Monte Carlo method (Gamborino et al., 2019; Wurz & Lammer, 2003). It is important to emphasize that our simulation results reflect a specific moment under moderate solar wind and radiation conditions. Any variation for the changes in driving conditions is not in the scope of this study.

In our simulation, we made several approximations and simplifications. First, we do not consider the energization of Na⁺ from ~eV to ~keV as the electric field was not included. We apply this approximation for the following two reasons: The plasma bulk velocity and the convection electric field in the dayside magnetosphere have yet to be measured directly. Furthermore, Aizawa et al. (2021) suggest the simulated convection electric field (Figure S5 in Supporting Information S1) in the dayside magnetosphere could be significantly contrasting in different global simulation models under the same upstream condition (northward interplanetary magnetic field, IMF). Our setting about the electric field is reasonable under northward IMF conditions as the dawn-dusk convection electric field is largely contributed by the solar wind motional electric field ($-\mathbf{v}_{sw} \times \mathbf{B}_{IMF}$) (Jasinski et al., 2017). In other words, our ionized Na atom dynamics simulation is more representative when the IMF is northward, corresponding to the period the FTE-shower is suppressed (Sun et al., 2020). In such a situation, the energization of Na⁺ might be attributed to the ion interaction with the dayside ultralow-frequency waves (James et al., 2016, 2019) instead of the pickup ion energization. No matter what energization process the Na⁺ experiences, this process takes time, and then our test particle simulation may underestimate the ion lifetime. On the other hand, the energization process can also result in ion precipitation, convection, and magnetopause shadowing, and we still cannot quantify the net effects. The test particle simulation results with an initial temperature of 100 eV are presented in Figure S6 of the Supporting Information S1 to illustrate a situation in which the Na⁺ ions are not fully energized at the first time (we take 100 eV as a reduced energy of the ions that energized from ~eV to 1 keV). In this simulation, the Na⁺ density in the dayside ring current is much higher as they sustain longer drift lifetimes.

Nevertheless, we can briefly discuss the potential influence on the Na⁺ dynamics from the electric field. Here, we include a Volland-Stern electric field within the closed field line region (Volland, 1978). In the magnetic equatorial plane, the model electric potential is given as $\sqrt{X^2 + Y^2 + Z^2} \cdot Y$ kV/R_M² (Figure 6a), corresponding to a ~20 kV dawn-dusk electric potential drop at $X = -3 R_M$ (Jasinski et al., 2017). The electric potential out of the magnetic equatorial plane is given through magnetic field line mapping in the KT17 model. Gray dashed lines in this panel represent the contour of the electric potential with a step of 1 kV. This model is capable of depicting the sunward convection in the inner magnetosphere region (from the low-altitude exosphere to the near-Mercury X-line). The electric potential drop between the subsolar and dawn/dusk sectors is about ~2 kV. Such a high

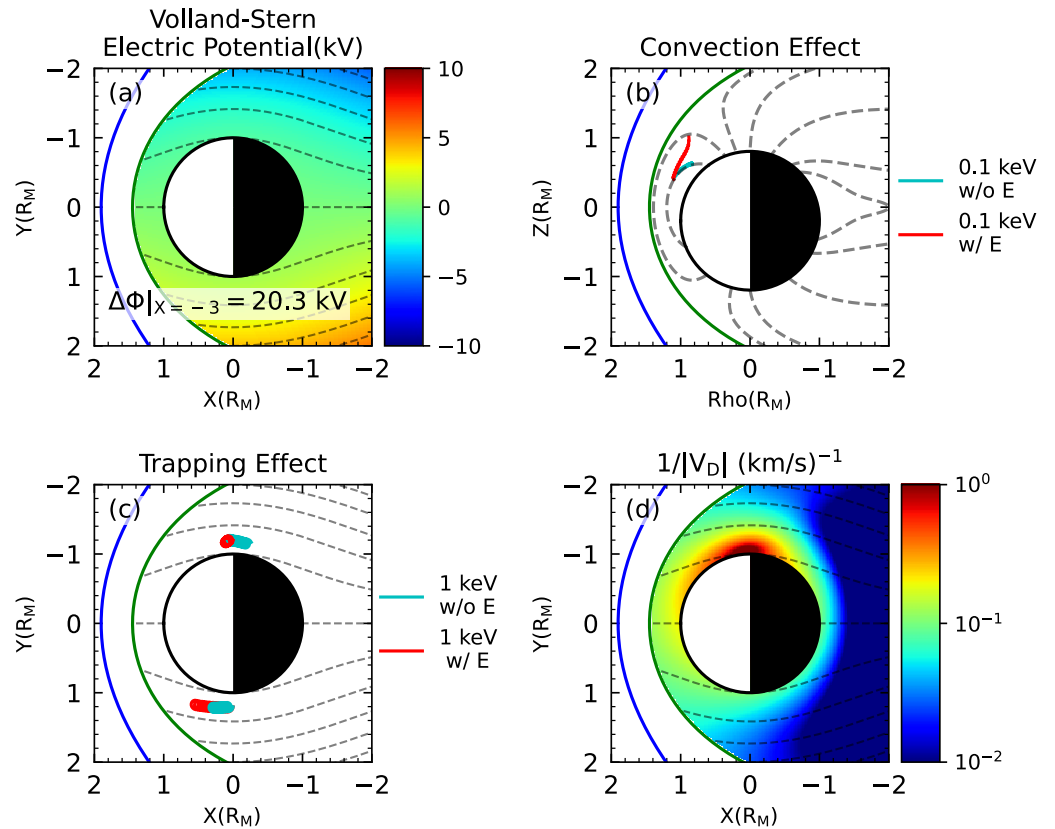


Figure 6. Test particle simulation result with the inclusion of a Volland-Stern electric field model. (a) The model electric field potential in the magnetic equatorial plane. (b) 0.1 keV Na^+ trajectories with (red) and without (cyan) the model electric field in the Rho-Z plane. (c) 1 keV Na^+ trajectories with (red) and without (cyan) the model electric field in the X-Y plane. (d) The inverse of the modeled drift velocity (gradient-curvature drift and $\mathbf{E} \times \mathbf{B}$ drift). Gray dashed lines in panels (a), (c), and (d) represent the contour of electric potential, and the gray dashed lines in panel (b) represent the model magnetic field lines.

potential drop suggests the 1 keV Na^+ ions with energy can no longer drift into the dawn sector if there is no other energization process. This is in contrast to the observation by MESSENGER of Na^+ in the dawn region. The following two panels show the electric field's influence on the Na^+ trajectory by full motion particle tracing ($m \frac{d^2\mathbf{r}}{dt^2} = q\mathbf{E} + q\mathbf{v} \times \mathbf{B}$). In Figure 6b, we present the convection effect caused by the model electric field. The duskward electric field in the magnetosphere drives the Na^+ 's poleward, cross-field convection (i.e., $\mathbf{E} \times \mathbf{B}$ drift, red solid line), while the Na^+ keeps moving along the magnetic field line when the electric field is not implemented (cyan solid line). This effect is especially significant for the low energy portion as their gradient-curvature drift velocity is less comparable to the $\mathbf{E} \times \mathbf{B}$ drift, and they may be swept to the polar cusp or plasma mantle instead of drifting to the dawn sector. In the dawn and dusk sector, the ion motion can be composited with the sunward $\mathbf{E} \times \mathbf{B}$ drift and the westward gradient-curvature drift. After including the convection electric field, the Na^+ ions will spend less of their lifetime in the dusk sector and more of their lifetime in the dawn sector, where the two kinds of drift cancel (Figure 6c) (Hao et al., 2020). This trapping effect can be evaluated through calculating the total drift velocity. Figure 6d presents the inverse of the drift velocity, and the dawn-dusk asymmetry in the trapping effect is also comparable to the asymmetry in the observed Na^+ density. It should be noted that the above Volland-Stern electric field model holds an electric potential drop that is even higher than the mean value (~ 19 kV) inferred from the H^+ dispersion pattern in the plasma mantle (Jasinski et al., 2017). Hence, this model represents an intense convection condition of the magnetosphere, but the realistic Na^+ ion dynamics may be less influenced in a southward IMF and non-FTE shower interval.

Another important dynamic process in the ion transport is the curvature scattering. For a Na^+ with 1 keV perpendicular energy, its gyro radius is 216 km within a 100 nT magnetic field. As a comparison, the minimal magnetic field curvature radius in the model for the dayside magnetosphere is 659 km (their positions are

indicated by the gray diamonds in Figure 5a). Given such a significant gyro-radius, it is plausible that the ion's pitch angle gets scattered due to field line curvature. At this point, we cannot rule out the potential cross-field transport of Na^+ toward regions like the polar cusp, ring current, magnetosheath, and loss cone. This scattering process has been involved in our full-Lorentz test particle simulation. However, a quantitative discussion about this process is not given in this study. This process might also provide insights into how cusp sodium enters the dayside ring current without any conflict with our scenario.

Overall, our simulation illustrates that the pre-ionization dynamic process of the sputtered neutral Na atoms can distribute Na^+ throughout various regions of the magnetosphere. The consistency between the observation and the simulation indicates the polar cusp sputtering atom, which is the only sodium source in our simulation, could be the most vital contributor to the $\sim\text{keV}$ Na^+ in the dayside magnetosphere.

5. Summary

We summarize our investigation into the following conclusions:

1. Although most sodium yield from solar wind sputtering is neutral, about 2.7% of these sputtered atoms ultimately contribute to the Na^+ in the magnetosphere.
2. Prior to the photoionization of sputtered neutral atoms, they can leave the polar cusps and move into other magnetosphere regions, such as the dayside ring current region, magnetotail lobe, and current sheet.
3. Our mechanism offers a novel understanding of the Na^+ entrance to the dayside ring current, which aligns with observed data and does not contradict any previously proposed mechanisms.

Data Availability Statement

MESSENGER data used in this study were available from the Planetary Data System (PDS): <http://pds.jpl.nasa.gov>; KT17 magnetic field model is available at <https://github.com/mattkames7/KT17>.

References

- Aizawa, S., Griton, L. S., Fatemi, S., Exner, W., Deca, J., Pantellini, F., et al. (2021). Cross-comparison of global simulation models applied to Mercury's dayside magnetosphere. *Planetary and Space Science*, 198, 105176. <https://doi.org/10.1016/j.pss.2021.105176>
- Alexeev, I. I., Belenkaya, E. S., Slavin, J. A., Korth, H., Anderson, B. J., Baker, D. N., et al. (2010). Mercury's magnetospheric magnetic field after the first two MESSENGER flybys. *Icarus*, 209(1), 23–39. <https://doi.org/10.1016/j.icarus.2010.01.024>
- Anderson, B. J., Acuña, M. H., Korth, H., Slavin, J. A., Uno, H., Johnson, C. L., et al. (2010). The magnetic field of Mercury. *Space Science Reviews*, 152(1–4), 307–339. <https://doi.org/10.1007/s11214-009-9544-3>
- Anderson, B. J., Johnson, C. L., Korth, H., Purucker, M. E., Winslow, R. M., Slavin, J. A., et al. (2011). The global magnetic field of Mercury from MESSENGER orbital observations. *Science*, 333(6051), 1859–1862. <https://doi.org/10.1126/science.1211001>
- Andrews, G. B., Zurbuchen, T. H., Mauk, B. H., Malcom, H., Fisk, L. A., Gloeckler, G., et al. (2007). The energetic particle and plasma spectrometer instrument on the MESSENGER spacecraft. *Space Science Reviews*, 131, 523–556. https://doi.org/10.1007/978-0-387-77214-1_15
- Cassidy, T. A., Merkel, A. W., Burger, M. H., Sarantos, M., Killen, R. M., McClintock, W. E., & Vervack, R. J. (2015). Mercury's seasonal sodium exosphere: MESSENGER orbital observations. *Icarus*, 248, 547–559. <https://doi.org/10.1016/j.icarus.2014.10.037>
- Delcourt, D. C., Grimald, S., Leblanc, F., Berthelier, J. J., Millilo, A., Mura, A., et al. (2003). A quantitative model of the planetary Na^+ contribution to Mercury's magnetosphere. *Annales Geophysicae*, 21(8), 1723–1736. <https://doi.org/10.5194/angeo-21-1723-2003>
- Delcourt, D. C., Moore, T. E., Orsini, S., Millilo, A., & Sauvaud, J. A. (2002). Centrifugal acceleration of ions near Mercury. *Geophysical Research Letters*, 29(12), 32-1–32-4. <https://doi.org/10.1029/2001GL013829>
- Delcourt, D. C., Seki, K., Terada, N., & Moore, T. E. (2012). Centrifugally stimulated exospheric ion escape at Mercury. *Geophysical Research Letters*, 39(22), L22105. <https://doi.org/10.1029/2012GL054085>
- Fu, S., & Zong, Q. (2022). Mercury's ring current and Mercury's magnetic storms. *Science China Technological Sciences*, 65(5), 1210–1212. <https://doi.org/10.1007/s11431-022-2010-4>
- Gamborino, D., Vorburger, A., & Wurz, P. (2019). Mercury's subsolar sodium exosphere: An ab initio calculation to interpret MASCS/UVVS observations from MESSENGER. *Annales Geophysicae*, 37(4), 455–470. <https://doi.org/10.5194/angeo-37-455-2019>
- Gershman, D. J., Raines, J. M., Slavin, J. A., Zurbuchen, T. H., Anderson, B. J., Korth, H., et al. (2015). MESSENGER observations of solar energetic electrons within Mercury's magnetosphere. *Journal of Geophysical Research: Space Physics*, 120(10), 8559–8571. <https://doi.org/10.1002/2015ja021610>
- Gershman, D. J., Slavin, J. A., Raines, J. M., Zurbuchen, T. H., Anderson, B. J., Korth, H., et al. (2014). Ion kinetic properties in Mercury's pre-midnight plasma sheet. *Geophysical Research Letters*, 41(16), 5740–5747. <https://doi.org/10.1002/2014gl060468>
- Glass, A. N., Raines, J. M., Jia, X., Tenishev, V., Shou, Y., Aizawa, S., & Slavin, J. A. (2021). A 3D MHD-particle tracing model of Na^+ energization on Mercury's dayside. *Journal of Geophysical Research: Space Physics*, 126(11), e2021JA029587. <https://doi.org/10.1029/2021JA029587>
- Glassmeier, K.-H., Auster, H.-U., & Motschmann, U. (2007). A feedback dynamo generating Mercury's magnetic field. *Geophysical Research Letters*, 34(22), L22201. <https://doi.org/10.1029/2007GL031662>

Acknowledgments

This work was supported by the National Natural Science Foundation of China 42230202 (QGZ), 42274200 (CY) and the Major Project of Chinese National Programs for Fundamental Research and Development 2021YFA0718600 (QGZ).

- Hao, Y. X., Sun, Y. X., Roussos, E., Liu, Y., Kollmann, P., Yuan, C. J., et al. (2020). The formation of Saturn's and Jupiter's electron radiation belts by magnetospheric electric fields. *The Astrophysical Journal Letters*, *905*(1), L10. <https://doi.org/10.3847/2041-8213/abca3f>
- Hofer, W. O. (1991). Angular, energy, and mass-distribution of sputtered particles. *Topics in Applied Physics*, *64*, 15–90. https://doi.org/10.1007/3540534288_16
- Ip, W. H. (1986). The sodium exosphere and magnetosphere of Mercury. *Geophysical Research Letters*, *13*(5), 423–426. <https://doi.org/10.1029/g1013i005p00423>
- James, M. K., Bunce, E. J., Yeoman, T. K., Imber, S. M., & Korth, H. (2016). A statistical survey of ultralow-frequency wave power and polarization in the Hermean magnetosphere. *Journal of Geophysical Research: Space Physics*, *121*(9), 8755–8772. <https://doi.org/10.1002/2016ja023103>
- James, M. K., Imber, S. M., Yeoman, T. K., & Bunce, E. J. (2019). Field line resonance in the Hermean magnetosphere: Structure and implications for plasma distribution. *Journal of Geophysical Research: Space Physics*, *124*(1), 211–228. <https://doi.org/10.1029/2018ja025920>
- Jasinski, J. M., Slavin, J. A., Raines, J. M., & DiBraccio, G. A. (2017). Mercury's solar wind interaction as characterized by magnetospheric plasma mantle observations with MESSENGER. *Journal of Geophysical Research: Space Physics*, *122*(12), 12153–12169. <https://doi.org/10.1002/2017ja024594>
- Korth, H., Johnson, C. L., Philpott, L., Tsyganenko, N. A., & Anderson, B. J. (2017). A dynamic model of Mercury's magnetospheric magnetic field. *Geophysical Research Letters*, *44*(20), 10147–10154. <https://doi.org/10.1002/2017gl074699>
- Mangano, V., Masetti, S., Milillo, A., Plainaki, C., Orsini, S., Rispoli, R., & Leblanc, F. (2015). THEMIS Na exosphere observations of Mercury and their correlation with in-situ magnetic field measurements by MESSENGER. *Planetary and Space Science*, *115*, 102–109. <https://doi.org/10.1016/j.pss.2015.04.001>
- Morrissey, L. S., Tucker, O. J., Killen, R. M., Nakhla, S., & Savin, D. W. (2022). Solar wind ion sputtering of sodium from silicates using molecular dynamics calculations of surface binding energies. *The Astrophysical Journal Letters*, *925*(1), L6. <https://doi.org/10.3847/2041-8213/ac42d8>
- Orsini, S., Mangano, V., Milillo, A., Plainaki, C., Mura, A., Raines, J. M., et al. (2018). Mercury sodium exospheric emission as a proxy for solar perturbations transit. *Scientific Reports*, *8*(1), 928. <https://doi.org/10.1038/s41598-018-19163-x>
- Raines, J. M., Gershman, D. J., Slavin, J. A., Zurbuchen, T. H., Korth, H., Anderson, B. J., & Solomon, S. C. (2014). Structure and dynamics of Mercury's magnetospheric cusp: MESSENGER measurements of protons and planetary ions. *Journal of Geophysical Research: Space Physics*, *119*(8), 6587–6602. <https://doi.org/10.1002/2014ja020120>
- Saito, Y., Sauvaud, J. A., Hirahara, M., Barabash, S., Delcourt, D., Takashima, T., & Asamura, K. (2010). Scientific objectives and instrumentation of Mercury Plasma Particle Experiment (MPPE) onboard MMO. *Planetary and Space Science*, *58*(1), 182–200. <https://doi.org/10.1016/j.pss.2008.06.003>
- Siscoe, G. L., Ness, N. F., & Yeates, C. M. (1975). Substorms on Mercury? *Journal of Geophysical Research (1896-1977)*, *80*(31), 4359–4363. <https://doi.org/10.1029/ja080i031p04359>
- Slavin, J. A., Acuna, M. H., Anderson, B. J., Baker, D. N., Benna, M., Boardsen, S. A., et al. (2009). MESSENGER observations of magnetic reconnection in Mercury's magnetosphere. *Science*, *324*(5927), 606–610. <https://doi.org/10.1126/science.1172011>
- Slavin, J. A., Anderson, B. J., Zurbuchen, T. H., Baker, D. N., Krimigis, S. M., Acuña, M. H., et al. (2009). MESSENGER observations of Mercury's magnetosphere during northward IMF. *Geophysical Research Letters*, *36*(2), L02101. <https://doi.org/10.1029/2008gl036158>
- Sun, W. J., Slavin, J. A., Milillo, A., Dewey, R. M., Orsini, S., Jia, X. Z., et al. (2022). MESSENGER observations of planetary ion enhancements at Mercury's northern magnetospheric cusp during flux transfer event showers. *Journal of Geophysical Research-Space Physics*, *127*(4), e2022JA030280.
- Sun, W. J., Slavin, J. A., Smith, A. W., Dewey, R. M., Poh, G. K., Jia, X., et al. (2020). Flux transfer event showers at Mercury: Dependence on plasma beta and magnetic shear and their contribution to the Dungey cycle. *Geophysical Research Letters*, *47*(21), e2020GL089784. <https://doi.org/10.1029/2020GL089784>
- Tsyganenko, N. A., & Russell, C. T. (1999). Magnetic signatures of the distant polar cusps: Observations by Polar and quantitative modeling. *Journal of Geophysical Research*, *104*(A11), 24939–24955. <https://doi.org/10.1029/1999ja000279>
- Volland, H. (1978). Model of magnetospheric electric convection field. *Journal of Geophysical Research*, *83*(6), 2695–2699. <https://doi.org/10.1029/ja083ia06p02695>
- Wang, Y. C., & Ip, W. H. (2011). Source dependency of exospheric sodium on Mercury. *Icarus*, *216*(2), 387–402. <https://doi.org/10.1016/j.icarus.2011.09.023>
- Wiens, R. C., Burnett, D. S., Calaway, W. F., Hansen, C. S., Lykke, K. R., & Pellin, M. J. (1997). Sputtering products of sodium sulfate: Implications for Io's surface and for sodium-bearing molecules in the Io Torus. *Icarus*, *128*(2), 386–397. <https://doi.org/10.1006/icar.1997.5758>
- Winslow, R. M., Anderson, B. J., Johnson, C. L., Slavin, J. A., Korth, H., Purucker, M. E., et al. (2013). Mercury's magnetopause and bow shock from MESSENGER magnetometer observations. *Journal of Geophysical Research: Space Physics*, *118*(5), 2213–2227. <https://doi.org/10.1002/jgra.50237>
- Wurz, P., Fatemi, S., Galli, A., Halekas, J., Harada, Y., Jaggi, N., et al. (2022). Particles and photons as drivers for particle release from the surfaces of the Moon and Mercury. *Space Science Reviews*, *218*(3), 10. <https://doi.org/10.1007/s11214-022-00875-6>
- Wurz, P., Gamborino, D., Vorburger, A., & Raines, J. M. (2019). Heavy ion composition of Mercury's magnetosphere. *Journal of Geophysical Research-Space Physics*, *124*(4), 2603–2612. <https://doi.org/10.1029/2018ja026319>
- Wurz, P., & Lammer, H. (2003). Monte-Carlo simulation of Mercury's exosphere. *Icarus*, *164*(1), 1–13. [https://doi.org/10.1016/s0019-1035\(03\)00123-4](https://doi.org/10.1016/s0019-1035(03)00123-4)
- Yoshikawa, I., Korabely, O., Kameda, S., Rees, D., Nozawa, H., Okano, S., et al. (2010). The Mercury sodium atmospheric spectral imager for the MMO spacecraft of Bepi-Colombo. *Planetary and Space Science*, *58*(1), 224–237. <https://doi.org/10.1016/j.pss.2008.07.008>
- Zhao, J. (2024). Sodium ion supply rate at different TAA. <https://doi.org/10.5281/zenodo.10662637>
- Zhao, J.-T., Zong, Q.-G., Slavin, J. A., Sun, W.-J., Zhou, X.-Z., Yue, C., et al. (2020). Proton properties in Mercury's magnetotail: A statistical study. *Geophysical Research Letters*, *47*(19), e88075. <https://doi.org/10.1029/2020gl088075>
- Zhao, J. T., Zong, Q. G., Yue, C., Sun, W. J., Zhang, H., Zhou, X. Z., et al. (2022). Observational evidence of ring current in the magnetosphere of Mercury. *Nature Communications*, *13*(1), 924. <https://doi.org/10.1038/s41467-022-28521-3>
- Ziegler, J. F., Ziegler, M. D., & Biersack, J. P. (2010). SRIM—The stopping and range of ions in matter (2010). *Nuclear Instruments & Methods in Physics Research Section B-Beam Interactions with Materials and Atoms*, *268*(11–12), 1818–1823. <https://doi.org/10.1016/j.nimb.2010.02.091>

- Zong, Q. G., Zhao, J. T., Liu, J. J., Fu, S. Y., Sun, W. J., Zhang, H., et al. (2022). Magnetic storms in Mercury's magnetosphere. *Science China Technological Sciences*, 65(6), 1427–1432. <https://doi.org/10.1007/s11431-022-2009-8>
- Zurbuchen, T. H., Raines, J. M., Gloeckler, G., Krimigis, S. M., Slavin, J. A., Koehn, P. L., et al. (2008). MESSENGER observations of the composition of Mercury's ionized exosphere and plasma environment. *Science*, 321(5885), 90–92. <https://doi.org/10.1126/science.1159314>
- Zurbuchen, T. H., Raines, J. M., Slavin, J. A., Gershman, D. J., Gilbert, J. A., Gloeckler, G., et al. (2011). MESSENGER observations of the spatial distribution of planetary ions near Mercury. *Science*, 333(6051), 1862–1865. <https://doi.org/10.1126/science.1211302>